

1 The Large Helical Device Vertical Neutron Camera Operating in the MHz Counting Rate Range

2

3 K. Ogawa^{1,2}, M. Isobe^{1,2}, T. Nishitani¹, and T. Kobuchi¹

4

5 1. National Institute for Fusion Science, National Institutes of Natural Sciences, Toki, Japan

6 2. SOKENDAI (The Graduate University for Advanced Studies), Toki, Japan

7

8 Email: kogawa@nifs.ac.jp

9

10 Abstract

11 In the currently performed neutral beam (NB) -heated deuterium plasma experiments, neutrons are
12 mainly produced by a beam-plasma reaction. Therefore, time-resolved measurement of the neutron
13 emission profile can enhance the understanding of the classical and/or anomalous transport of beam
14 ions. To measure radial neutron emission profiles as a function of time, the vertical neutron camera
15 (VNC) capable of operation with a counting rate in the MHz range was newly installed on the Large
16 Helical Device (LHD). This is the world's first neutron camera for stellarator/heliotron devices. The
17 VNC consists of a multichannel collimator, eleven fast-neutron detectors, and the digital-signal-
18 processing-based data acquisition system (DAQ). The multichannel collimator having little crosstalk

19 was made from hematite-doped heavy concrete, which has a high shielding performance against both
20 neutrons and gamma-rays. A stilbene crystal coupled with a photomultiplier having high-gain-stability
21 in the high-count rate regime was utilized as a fast-neutron scintillation detector because it has a high
22 neutron-gamma discrimination capability at high count rates. The DAQ system equipped with a field
23 programmable logic controller was developed to obtain the waveform acquired with a 1 GHz sampling
24 rate and the shaping parameter of each pulse simultaneously at up to 10^6 cps (counts per second).
25 Neutron emission profiles were successfully obtained in the first deuterium campaign of LHD in 2017.
26 The neutron emission profile was measured in tangentially co-injected NB-heated plasma with
27 different magnetic axes (R_{ax}). The neutron counts became larger in the inward-shifted configuration,
28 which was consistent with the total neutron rate measured by the neutron flux monitor. The radial peak
29 position of the line-integrated neutron profile which changed according to R_{ax} showed that the VNC
30 worked successfully as designed. The VNC demonstrated the expected performance conducive to
31 extending energetic-particle physics studies in LHD.

32

33 Keywords: Large Helical Device, Neutron Camera, Fast-neutron Detection

34

35 I. Introduction

36 Neutron diagnostics have been developed because neutron measurement is one of the key methods in

37 order to obtain the fusion output power directly from a fusion burning plasma.¹ In deuterium plasmas,
38 2.45 MeV neutrons are produced as a result of the $d(d,n)^3\text{He}$ reactions. The spatially-resolved
39 measurement of fusion neutron emission from the currently performed plasma experiment supports
40 the theoretical modeling of the plasma, which preindicates the plasma behavior in a fusion reactor. In
41 most of the currently performed neutral beam (NB) heated plasma experiments, neutrons are mainly
42 created by the reactions between thermal plasma and beam ions. Therefore, neutron diagnostics have
43 mainly been utilized to study the energetic ion behavior. The measurement of the neutron emission
44 profile was reported for the first time in Princeton Large Torus (PLT) using nuclear emulsions in 1978.²
45 The shot integrated neutron emission profile matched the theoretical model based on the Fokker-
46 Planck equation under the total neutron emission rate of 10^{12} n/s. In the 1980s, the measurement of
47 the time evolution of the neutron emission profile was possible using neutron cameras mainly
48 composed of a multichannel collimator and fast-neutron detectors because the total neutron emission
49 rate increased by more than a factor of four with the increase of the plasma performance.
50 Neutron cameras were installed and have been working since the late 1980s in large tokamaks. The
51 vertical neutron camera (VNC) having the right cylinder type collimator was installed in the basement
52 of the Tokamak Fusion Test Reactor (TFTR).^{3,4} The multichannel collimator was made of brick and
53 lead block stacked above the fast-neutron detectors. They used a zinc sulfide phosphor embedded in a
54 hydrogenous polymer matrix scintillator (NE451) operated in the current mode. The neutron camera

55 indicates that the peak of the line-integrated neutron emission profile agrees with the plasma axis as
56 expected by transport code TRANSP.³ Horizontal and vertical neutron cameras were installed in the
57 Joint European Torus (JET).^{5,6} Two multichannel collimators, made from barite-doped heavy concrete
58 with a mass density of around 3.5 g/cm³, are placed on the upper side and the outboard side of the
59 plasma. The liquid scintillator (NE213) with the analogue-circuit-based pulse shape discrimination
60 circuit was used and recently upgraded to the FPGA-based pulse shape discrimination circuit.⁷
61 Tomography of the neutron emission profile is performed using both horizontal and vertical cameras.⁸
62 Neutron cameras with six sight lines were installed on the outboard side of the JAERI Tokamak 60
63 Upgrade (JT-60U).⁹ They used multichannel collimators made from polyethylene and lead. The
64 stilbene scintillator with the analogue-circuit-based pulse shape discrimination circuit was previously
65 used. The circuit was upgraded to the flash ADC modules.¹⁰ The energetic ion transport due to the
66 energetic particle mode is observed with the neutron camera¹¹. In middle size tokamaks, the neutron
67 cameras are installed in FTU¹², MAST¹³, KSTAR^{14, 15}, EAST¹⁶, HL-2A¹⁷, and MST¹⁸, and are used to
68 understand the energetic particle transport and losses.¹⁹ In ITER, the installation of vertical and
69 horizontal neutron cameras is planned.^{20,21} In helical devices and stellarators, no neutron cameras have
70 been installed because the neutron emission rate in previous experimental devices was too low to
71 measure the neutron emission profile. The deuterium operation of the LHD makes it feasible to obtain
72 time-resolved measurements of the neutron emission profile from the plasma because the expected

73 neutron emission rate from the NB-heated deuterium LHD plasma is 10^{16} n/s order which is equivalent
74 to the neutron emission rate of the deuterium operation of large tokamaks. The plan for installation of
75 the VNC was initiated during the construction phase of the LHD.²² The height of the multichannel
76 collimator composed of polyethylene was studied by the MCNP5 code.²³ It was reported that a sharp
77 peak of DD neutrons can be recognized when the collimator length is set to be 1.5 m. Through the
78 study of the multichannel collimator design, progress was made in fast-neutron detection systems.²⁴ A
79 multichannel collimator made of heavy concrete and a Stilbene scintillation detector were suggested,
80 however the design of a fast-neutron detection system operating with 10^6 cps was not completed.²⁵
81 This paper describes the design and performance of the VNC stably operated with 10^6 cps, which is
82 now used regularly to measure the time evolution of the neutron emission profile during LHD
83 discharges.

84

85 II. Design of the vertical neutron camera

86 II-1 General outline

87 The VNC installed in the basement of the LHD torus hall sees the plasma from the lower side (Fig. 1).

88 The VNC mainly consists of three parts: a multichannel collimator, fast-neutron scintillation detectors,
89 and the digital-signal-processing-based data acquisition system. The VNC has a right cylinder
90 collimator type, similar to the neutron camera installed in TFTR and views the radial profile of neutron

91 emission with eleven sight lines. The geometry ensures that each individual collimator channel has the
92 same viewing efficiency. The distance from the plasma center to the multichannel collimator front and
93 the fast-neutron detector are 5.5 m and 8.5 m, respectively. Eleven ICF70 ports aligned to the axis of
94 the collimator were installed on the lower port of LHD. The thickness of the central part of the ICF70
95 flange is reduced to 2 mm in order to reduce the neutron scattering.

96

97 II-2 Multichannel collimator

98 The multichannel collimator is installed in the LHD torus hall concrete floor with a thickness of 2000
99 mm (Fig. 2). The hole created in the concrete floor has a rectangular shape. The size of the bottom
100 opening is 1400 mm in depth (major radial direction) and 800 mm in width. The height of the
101 multichannel collimator was determined to be 1500 mm in order to implement sufficient shielding
102 ability as evaluated using the neutron transport calculation.^{23,24} The collimator support was made using
103 angle bars made of SUS304A having a height of 250 mm, a width of 100 mm and a thickness of 10
104 mm for fixing the vertical rib plate. The structure of the collimator support was designed based on a
105 structural calculation. The collimator support is fixed with an M20 adhesive anchor and the gap
106 between the angle bars and the floor concrete is filled by shrinkage-compensating mortar in order to
107 avoid water and concrete falling to the understructure. The multichannel collimator is made using the
108 hematite (Fe_2O_3)-doped heavy concrete. The mass density of heavy concrete is 3.5 g/cm^3 , which is

109 almost the same as the mass density of the heavy concrete used for the multichannel collimator of the
110 JET neutron camera. We used 210 kg of water, 380 kg of cement, 2100 kg of hematite with a particle
111 size of 2 mm, and 3700 kg of hematite with a particle size of 20 mm. The composition of heavy
112 concrete is shown in Table 1. Note that the reason for using the heavy concrete is that the heavy
113 concrete collimator has better performance in reducing unwanted gamma-rays compared with
114 collimators made of polyethylene and lead according to the Monte Carlo neutron and gamma-ray
115 transport calculation.²⁴

116 The collimator consists of 3 sub-sections of 500 mm high stainless steel (SUS304A) pipes embedded
117 in heavy concrete. The three collimator units are stacked on the collimator support, and then the gap
118 between collimator units and the floor concrete is filled with heavy concrete. Here, we caulked the
119 small gap between collimator unit and collimator support to avoid water leakage. The reason for
120 making three collimator units is in order to avoid the bending of relatively long stainless steel pipes
121 due to the high pressure from the heavy concrete. Here, the size of the collimator unit placed on the
122 top is slightly smaller than that of the others in order to obtain easier access to the lower region during
123 the concrete placing work. The total weight of the heavy concrete used for the multichannel collimator
124 is approximately seven tons. In addition to the heavy concrete collimator, lead with a thickness of 150
125 mm (30 sheets of t of 5 mm lead plate) is placed under the heavy concrete collimator in order to reduce
126 the unwanted gamma-ray. Note that holes with a diameter of 30 mm are made in the lead sheets along

127 the sight lines to avoid the neutron scattering. The VNC has eleven sight lines whose inner diameter
128 is 30 mm aligned radially. A sight line is placed at each R of 3.36 m, 3.45 m, 3.54 m, 3.63 m, 3.72 m,
129 3.81 m, 3.90 m, 3.99 m, 4.08 m, 4.17 m, and 4.26 m. The distance between the centers of two sight
130 lines is 90 mm. Note that the inner diameter of the sight line can be changed to 10 mm or 20 mm using
131 an additional stainless steel pipe with the length of 500 mm. It should be pointed out that the relatively
132 short length of the additional stainless pipe is to avoid having a smaller pipe become stuck inside a
133 larger pipe. Fast-neutron detectors are placed at the bottom of the multichannel collimator. The support
134 of neutron detectors is designed to accept a supporting a weight of 500 kg. The crosstalk of the
135 multichannel collimator is experimentally obtained by using an intensive ^{252}Cf neutron source. The
136 experimental results indicate that the crosstalk of the multichannel collimator is approximately 1 %.²⁶
137 Figure 3 shows the sight line of the VNC together with the poloidal cross section of the plasmas having
138 the magnetic axis positions (R_{ax}) of 3.60 m and 3.90 m. The figure shows that the VNC is designed to
139 cover of the entire plasma region and obtain the information about the plasma axis position. Here, the
140 sight line with R of 4.26 m is designed in order to obtain the background counts. The plasma visible
141 region through sight line is approximately a cylinder with a 88 mm diameter at the bottom of the
142 plasma and a 110 mm diameter at the top of the plasma for the central cord (R of 3.63 m) and the
143 volume of the visible region is 0.05 m^3 .
144

145 II-3 Fast-neutron detection system

146 The block diagram of the fast-neutron detection system is illustrated in Fig. 4 (a). We choose a stilbene
147 scintillator directly coupled with the PMT (H11934-100-10MOD²⁷ with a 3 m cable) having high gain
148 stability as a fast-neutron detector. The typical rise and transit time of the PMT are 1.3 ns and 5.8 ns,
149 respectively. The signal from the fast-neutron detector is directly fed into the data acquisition system.
150 The length of the co-axial cable (3D-FB²⁸) from the detector to the data acquisition system is 18 m.
151 The length of the cable is decided by the possible locations for installing the Fast-neutron detection
152 system and the effect of the cable length on signal. We evaluated the effect of the cable length on the
153 pulse height and width using an LED emitting green light. Here, the pulse width of the LED light is
154 20 ns. The data acquisition system should be placed away from the machine to prevent radiation
155 damage of the data acquisition system. However, the long cable causes a reduction of the signal height
156 and the broad signal. Therefore, the effect of the cable length on the pulse signal was investigated.
157 Figure 4 (b) shows the pulse height and width measured by an Oscilloscope (DPO 7104C²⁹, Tektronix)
158 as a function of the cable length. The pulse height gradually decreases and the pulse width gradually
159 expended with the increase of the capacitance of the cable, as expected. The pulse height decreases by
160 25 % at the cable length of around 50 m and the pulse width becomes 30 % wider at the cable length
161 of around 40 m compared with a 3 m cable (no cable extension). It is found that on the VNC the pulse
162 height decreases by 10 % and the pulse width becomes wider by 11 % with an 18 m cable compared

163 with a 3 m cable. On the other hand, the pulse height decreases by 40 % and the pulse width becomes
164 wider by 50 % with a 100 m cable. The data acquisition system for the VNC is placed on the basement
165 level of the torus hall (cable length of 18 m) rather than in the data acquisition room located outside
166 of the torus hall (100 m) because 40 % smaller means that the signal to noise ratio becomes a 40 %
167 less and a 50 % wider signal induces a 50 % higher pile up rate. The data acquisition system
168 (APV8102-14MWPSAGb³⁰, Techno AP) composed of the fast digitizer, a leading edge technology
169 field programmable logic circuit, and synchronous dynamic random access memory (SDRAM), is
170 developed for the LHD VNC. High voltage is applied using an externally controllable high voltage
171 power supply with logging function (APV3304³¹, Techno AP). We can obtain the information of both
172 applied voltage and supplied current every 1 ms to monitor the gain variation of the PMT. The
173 maximum voltage and current of APV3304 is 1 kV and 4 mA, respectively. In addition to the primary
174 high voltage module, external DC power supplies (P4K80H³², Matsusada Precision) are additionally
175 prepared in order to suppress the gain shift of the PMT in the high counting rate regime. The maximum
176 voltage, current, and power of P4K80H are 320 V, 0.5 A, and 80 W, respectively. The Ethernet outputs
177 of these modules are gathered to the high-speed Ethernet hub (XS712³³, NETGEAR Corp.) equipped
178 with an SFP+ port. The SFP+ port is connected to the data acquisition PC through a 10 Gbps network.
179 Because the minimum operation interval of the LHD is approximately three minutes and the maximum
180 stored data of the DAQ is 11 GB, the required average transfer rate of the data acquisition system is

181 more than 500 Mbps. Therefore, we choose the 10 Gbps network for the data transfer. To acquire such
182 large data with high speed, we choose a relatively high performance data acquisition server equipped
183 with Xeon E5-2603v3 $\times 2$ CPUs, 32 GB DDR4 ECC Registered memory, Intel Ethernet SFP+, and
184 SSD (SSDSC2KW240H6X1) $\times 3$ RAID0. The specification of each component in detail will be
185 described in the next section.

186

187 III Experimental system

188 III-1 Magnetic shield for fast-neutron detector

189 The neutron detector must work under a relatively strong magnetic field environment, however the
190 effect of neutron scattering due to the magnetic shield should be reduced. The goal was to design the
191 magnetic shield surrounding the PMT without front and back sides in order to reduce the neutron
192 scattering. The fast-neutron detector shown in Fig. 5 is composed of the magnetic shield, the stilbene
193 scintillator, and the photomultiplier. Because the photomultiplier (PMT) is sensitive to the magnetic
194 field, we need the magnetic shield in order to reduce the magnetic field strength to an acceptable value.
195 The acceptable magnetic field for the PMT used for the LHD VNC is approx. 0.05 mT. Figure 6 (a)
196 shows the profile of the magnetic field strength at the standard configuration of the LHD experiment
197 at R of 3.60 m. Here, the toroidal magnetic field strength (B_t) is 3 T and R_{ax} is 3.60 m and $Z = 0$
198 corresponds to the plasma axis position. The figure shows that the magnetic field strength of the fast-

199 neutron detector position at $Z = 8$ m is around 12 mT in the radial direction and 6 mT in the vertical
200 direction. It is notable that the toroidal magnetic field component is negligibly small compared with
201 the radial magnetic field component. We designed the magnetic shield with a 1 mm thickness of
202 Permalloy C surrounded by a 10 mm thickness of SS400 using the finite element method. The length
203 of the magnetic shield is 300 mm and the photomultiplier tube is located at the center of the magnetic
204 shield. We designed a relatively long magnetic shield so that no magnetic shield component is located
205 on the front and the back of the fast-neutron detector in order to avoid the scattering of fast-neutron
206 due to the magnetic shield. We should keep in mind that the weight of the magnetic shield is
207 approximately 10 kg. The performance of the magnetic shield was checked by an experiment using a
208 light emitted diode (LED) in the magnetic field produced by HYPER-I.³⁴ HYPER-I is the linear high-
209 density plasma device which can produce a linear magnetic field up to 250 mT. The PMT surrounded
210 by magnetic shield was placed parallel /perpendicular to the axis of HYPER-I. An LED fixed in front
211 of the PMT emits a light using a function generator (WF1946³⁵, NF Corporation) with a pulse rate of
212 100 Hz and pulse width of 30 ns. We changed the magnetic field strength and recorded the pulse height
213 of the PMT signal measured by an Oscilloscope (DPO 7104C, Tektronix). The pulse height as a
214 function of the magnetic field strength is shown in Fig. 6 (b). Here, z is defined along the central axis
215 of the PMT and x and y are perpendicular to the z axis. The dependence of the pulse height as a
216 function of the magnetic field strength shows that the pulse height stays constant in the B_x and B_y cases,

217 whereas the pulse height decreases from B of 0.04 T in the B_z case. The design of a magnetic shield
218 having minimal neutron scattering effect and working in the VNC position (B_R of around 12 mT and
219 B_z of 6 mT) was completed.

220

221 III-2 Gain stability of PMT in high-counting rate region

222 The understanding on the characteristics of the PMT in the high counting rate regime is one issue for
223 stable operation of the neutron measurement, especially in the neutron and gamma-ray discrimination.

224 In JT60-U, the gain shift of the PMT caused a disturbance on the neutron and gamma-ray
225 discrimination plot.³⁶ The goal of the PMT development is no gain shift in MHz pulse rate region. The

226 PMT used for the fast-neutron detector of the LHD VNC has a metal channel dynode structure and
227 consists of twelve stages. The maximum applied high voltage and typical gain are -1000 V and 4.8×10^5 ,

228 respectively. High voltage cables and 0.01 F capacitors are connected to the last three dynodes of the

229 PMT. Each high voltage cable is connected to an external voltage module. In the high counting rate
230 region, these external DC power supplies supply the current in order to sustain the high voltage in the

231 latter phase of the dynodes for suppressing gain variation in the high counting rate condition. The gain

232 stability of the PMT was checked by using two LED lights emitting green light. The experimental
233 setup is shown in Fig. 7(a). Two LEDs were fixed in front of the PMT placed in a dark room. One

234 LED called LED1 emitted a light with 100 Hz, whereas the frequency of the other LED called LED2

235 was changed from 300 Hz to 10^6 Hz. We measured the pulse height of the PMT signal created by
236 LED1 light by an Oscilloscope (DPO 7104C, Tektronix). Here, the pulse height and width created by
237 LEDs are around 200 mV and 30 ns, respectively in the case of a high voltage of 700 V, which is
238 similar to the pulse height of a 2.45 MeV neutron signal of the fast-neutron detector. Figure 7 (b)
239 shows the pulse height created by LED1 as a function of the pulse rate of LED2. The pulse heights in
240 the case of the high voltages of 700 V and 800 V are 200 mV and 600 mV, respectively. The gain of
241 the PMT at 700 V and at 800 V are 4.0×10^4 and 1.5×10^5 , respectively. It is worth noting that the gain
242 shift occurred at a different pulse rate in each case. The gain shift of the PMT occurred depending on
243 the ratio of the signal current on the dynode current. When the signal current becomes not negligible
244 with respect to the dynode current, a gain shift occurred due to the decrease of the voltage between
245 dynodes of the PMT. The signal current of the PMT increases nonlinearly with high voltage, whereas
246 the dynode current increases linearly with the high voltage. Therefore, the saturation level becomes
247 lower in the 800 V case compared with the 700 V case because the ratio of the signal current on the
248 dynode current is higher. In the case of a high voltage of 700 V, without external DC power supplies,
249 the pulse height increases from around the pulse rate of 10^5 Hz and then decreases starting from 3×10^5
250 Hz, whereas the pulse height is almost constant regardless of the pulse rate of LED2 with external DC
251 power supplies. In the case of a high voltage of 800 V, without external DC power supplies, the pulse
252 height increases at a pulse rate of LED2 of 10^3 Hz and then decreases monotonically with respect to

253 the pulse rate of LED2, whereas the pulse height is almost constant irrespective of the pulse rate of
254 LED2 with external DC power supplies. The experimental results show that the external DC power
255 supplies works successfully to suppress the gain variation and the gain of the fast-neutron detector is
256 stable under the pulse rate of 10^6 Hz. The PMT suitable for the Stilbene fast-neutron detector stably
257 operated at a 10^6 pulse rate without gain variation was developed.

258

259 III-3 Digital signal processing unit

260 The DAQ system (APV8102-14MWPSAGb) for the VNC is newly developed by combining a high-
261 speed sampling rate analog to digital converter (1 GHz sampling, 14 bits and 2 or 6 V_{pp}) and a field
262 programmable logic circuit (Fig. 8a) in order to accept the superior performance of fast-neutron
263 detector operating in the 10^6 pulse rate regime. Figure 8 (b) is a block diagram of the DAQ board. The
264 signal acquired by the high speed ADC is transferred to the FPGA. The FPGA judges whether the
265 signal is above the threshold value. If the signal exceeds the threshold value, the time stamp is recorded
266 by using the constant fraction discriminator (CFD) function. Then, signal integrations Q_{total} and Q_{long}
267 are calculated. At the same time, the raw waveform consisting of 64 points is stored in the 1 GB
268 SDRAM. After the discharge, all the data is transferred to a PC through the Ethernet. Here, the data
269 size of each pulse is 144 Bytes. Therefore, the expected data transfer rate at the 10^6 cps counting rate
270 is ~ 1.2 Gbps per channel. Then we choose DDR2 SDRAM because of its high data transfer rate of

271 more than 3 Gbps. The DAQ only stored meaningful pulses. The acquisition time is not limited by the
272 duration of the acquisition but by the number of pulses. The maximum number of pulses stored in the
273 board is designed to be 3×10^6 per channel, because of the maximum expected neutron counts on an
274 LHD discharge (10^6 cps \times 3 seconds).

275

276 IV Characteristics of Fast-neutron detection system

277 IV-1 Optimal t_{fast} for pulse shape discrimination

278 Pulse shape discrimination (PSD) is performed using the expression $\text{PSD} = Q_{\text{long}} / Q_{\text{total}}$. Here, Q_{total}
279 represents integration of the signal from the beginning to the end of the stored waveform of 64 ns
280 length, whereas Q_{long} represents the integration of the signal from an arbitrary time in the middle of
281 the signal, t_{fast} , to the end. As shown in Fig. 9(a), neutron induced signal has a longer decay time, and
282 then the PSD becomes larger compared with the PSD of gamma-ray induced signal. We evaluated the
283 pulse shape discrimination ability using a ^{252}Cf neutron source in order to obtain the optimal t_{fast} .
284 Figure 9(a) shows the typical waveform acquired by APV8102-14MWPSAGb. Figure 9 (b) shows the
285 pulse shape discrimination result of stilbene detectors at t_{fast} of 20 ns. We surveyed the pulse shape
286 discrimination ability as a function of t_{fast} . Here, we used the Figure of Merit (FOM) as an index of the
287 pulse shape discrimination ability. The FOM is defined as $\text{FOM} = (\text{PSD}_{\text{peak}}(\text{neutron}) -$
288 $\text{PSD}_{\text{peak}}(\text{gamma-ray})) / (\text{FWHM}(\text{neutron}) + \text{FWHM}(\text{gamma-ray}))$, where FWHM indicates the full

289 width at half maximum. A non-zero FOM appears from t_{fast} of 17 ns, has a peak around 20 ns, and
290 decreases from t_{fast} of 22 ns. It should be pointed out that no FOM was obtained when t_{fast} was less
291 than 17 ns because only one peak appeared. Therefore, it is found that the optimal t_{fast} for this fast-
292 neutron detector is around 20 ns.

293

294 IV-2 PSD capability in high counting rate

295 The DD neutron measurement using the fast-neutron detector is performed using an accelerator-based
296 neutron generator on the Fast Neutron Source (FNS) in the Japan Atomic Energy Agency³⁷. The DD
297 neutrons are generated due to the deuteron beam and the deuterium target reaction. The typical neutron
298 emission rate from the target is 10^9 neutrons per second. We used an x-axis stage (KXL06300³⁸, Suruga
299 Seiki CO.,LTD.) in order to change the neutron flux at the detector position by changing the distance
300 from the target to the detector. Note that the neutron flux at the detector position is from $2.5 \times 10^6 \text{ cm}^{-2}$
301 s^{-1} to $2.2 \times 10^7 \text{ cm}^{-2} \text{ s}^{-1}$. The fast-neutron detector is placed in front of the DD neutron target. The energy
302 of the DD neutron is around 3 MeV. Figure 10 shows the two dimensional pulse shape discrimination
303 plot at the pulse counting rate of 108 kcps to 911 kcps. Here, the total number of pulses of each run
304 are 3×10^6 . Two peaks corresponding to the neutron and gamma-ray are clearly separated. It is
305 important to note that the pulse shape discrimination map does not change as expected from the
306 characteristics of the PMT gain stability reported in Sec II-2. Here, we can see several points on the

307 left and the right hand side of the two dimensional plot; this is due to the pile-up of pulses. The number
308 of these plots increases with the increase of the counting rate as expected by the simple pile up
309 calculation ($n/(1-nt_{\text{pulse}})$): n and t_{pulse} represent the counting rate of the pulse measured by the ADC and
310 the total width of the pulse, respectively. The larger PSD is obtained when the second pulse comes
311 after t_{fast} , whereas when the second pulse is coming before t_{fast} , the smaller PSD is obtained. The
312 number of pulses acquired by the DAQ as a function of the expected pulse counting rate evaluated by
313 the neutron flux is shown in Fig. 11. Here, we compared three different digitizers: DT5751³⁹ CAEN,
314 NI5772⁴⁰+PXIe-7962R⁴¹ National Instruments, and APV8102-14MWPSAGb Techno AP. DT5751
315 has 10 bits, 1 GHz, and 1 V_{pp} and only online analysis based on Q_{long} and Q_{short} is possible.
316 NI5772+PXIe-7962R reported in Ref. 23 has 12 bits, 1.6 GHz, equipped with 512 DDR2 SDRAM
317 memory and either online analysis or offline analysis (stored waveforms) is possible. It is should be
318 emphasized that those three DAQs acquire the periodic pulses with 10^6 pulses per second without any
319 loss of pulses. The loss of pulses occurred when the expected counting rate was around 8×10^5 cps.
320 Here, the counting rate of the ADC compensates with simple pile-up theory. The pulse loss ratio of
321 DT5751, NI5772+PXIe-7962R, and APV8102-14MWPSAGb at 10^6 cps are around 12 %, 16 %, and
322 8 %, respectively. It is found that the highest counting resistance among these three DAQs APV8102-
323 14MWPSAGb.
324

325 IV-3 Detection efficiency and detector response

326 The detection efficiency and the detector response of the fast-neutron detector are obtained at the Fast
327 Neutron Laboratory (FNL)⁴² of Tohoku University, at FNS, and at the Intense 14 MeV Neutron Source
328 Facility (OKTAVIAN)⁴³ of Osaka University. We used the p-Li reaction in order to produce neutrons
329 having an energy of 1.3 MeV in FNL, d-D reaction for 3 MeV neutrons in FNS, d-D reaction for 4.5
330 MeV to 5.7 MeV neutrons in FNL, and d-T reaction for 14 MeV neutrons in OKTAVIAN. Figure 12(a)
331 shows the pulse height spectra of the fast-neutron detector. Note that the threshold value in the case of
332 a neutron energy of 1.3 MeV and the threshold value in the other case are 10 mV and 30 mV,
333 respectively. The lower threshold value in the case of the neutron energy of 1.3 MeV is for observing
334 the response of the lower energy neutrons. Here, pulse height is evaluated by the waveform data. The
335 pulse height becomes larger with the increase of the neutron energy, as expected. Figure 12(b) shows
336 the maximum pulse height as a function of neutron energy. The plot shows that we can measure fast
337 neutrons having an energy of around 2 MeV if the threshold value is set to be 30 mV. We evaluated
338 the counting efficiency using an In foil in the FNS experiment. In this experiment, the In foil was
339 placed in front of the Stilbene detector and the time evolution of the neutron emission rate was
340 evaluated by a beam current monitor. Here, the distance between the deuterium target and the Stilbene
341 detector was 10 cm. It was found that the counting efficiency of the Stilbene detector is 0.06
342 counts/neutron/cm², for 3 MeV neutrons with high voltage of 700 V and threshold setting of 30 mV.

343

344 V Typical data of the LHD experiment

345 Measurement of the time evolution of the neutron emission profile is performed in the LHD deuterium

346 operation (Fig. 13). In this discharge, B_t is 2.75 T and R_{ax} is 3.60 m. Electron cyclotron heating and a

347 negative-ion-based NB injection are started at the time $t = 3.3$ s. Thomson scattering diagnostics⁴⁴

348 measure the central electron temperature and the line-averaged electron density is measured by an

349 interferometer⁴⁵. The total neutron emission rate (S_n) measured by the absolutely calibrated neutron

350 flux monitor⁴⁶ gradually increases due to NB injections. Figure 14(a) shows the pulse shape

351 discrimination result of channel 4 (R of 3.63 m). The two peaks are clearly separated at a PSD of 0.175.

352 In this discharge, the number of neutron counts is 3500, whereas the number of gamma-ray counts is

353 17000. The time evolution of the line-integrated neutron profile shows almost a similar trend with S_n

354 as shown in Fig. 14(b). The neutron emission profiles are obtained in different R_{ax} configurations (Fig.

355 14 (c)). As R_{ax} shifts outward, neutron counts decrease due to the decrease of S_n . In addition, the peak

356 of the line-integrated neutron emission profile shifts outward with R_{ax} , as expected. We showed that

357 the VNC is installed with the desired performance. The VNC will be a powerful tool to measure the

358 neutron emission profile in LHD.

359

360 VI Summary

361 The vertical neutron camera characterized by high-counting rate capability is developed for LHD
362 deuterium operation in order to understand the beam ion behavior. A multichannel collimator was
363 constructed with hematite-doped heavy concrete. The magnetic shield is designed based on a finite
364 element method by considering the magnetic field strength at the VNC position. We experimentally
365 showed that the magnetic shield is manufactured according to the design requirements. The fast-
366 neutron detector composed of a stilbene scintillator characterized by high pulse shape discrimination
367 ability coupled with the PMT characterized by high gain stability equipped with external DC power
368 supplies for further improved gain stability were installed. The test of the high gain stability of the
369 PMT using an LED shows that external DC power supplies are effective for suppressing the gain
370 variation and the gain of the PMT is constant up to the pulse rate of 10^6 Hz. The DAQ composed of
371 the fast ADC and the novel logic circuit realized in the FPGA enable us to obtain data needed for
372 online and offline analysis simultaneously. The neutron measurement was performed on accelerators
373 using p-Li, d-D, and d-T reactions. It is found that the two dimensional pulse shape discrimination
374 map does not change even in the 10^6 cps region. The counting loss of the pulse under the 10^6 cps is
375 8 %, which is the smallest value compared with other digitizers like DT5751 and NI5772+PXIe-7962R.
376 The response of the fast-neutron detector shows that the detector can measure the neutron energy from
377 around 2 MeV when the discrimination level is set to be 30 mV. Initial measurement of the line-
378 integrated neutron emission profile was performed in LHD deuterium operation in order to check the

379 expected performance of the VNC. The time-resolved neutron emission profile has a time trend similar
380 to the total neutron emission rate. The typical neutron, gamma-ray ratio is 1:5 for the central channel.
381 The measurement of the neutron emission profile at R_{ax} of 3.60 m and of 3.90 m shows that the peak
382 of the line-integrated neutron emission profile shifts according to the R_{ax} position as expected.

383

384 Acknowledgments

385 This research was supported by NIFS Collaboration Research programs (KOA033), by the LHD
386 project budget (ULHH003, ULHH034, ULHH802, and ULGG801), and Japan/U.S. Cooperation in
387 Fusion Research and Development. One of the authors, K. Ogawa, is pleased to acknowledge the
388 assistance of LHD Experiment Group for assistance in installation and operation of the VNC; K.
389 Ochiai and the FNS team of National Institutes for Quantum and Radiological Science and
390 Technology, M. Miwa, S. Matsuyama, and the FNL team of Tohoku University, and I. Murata of the
391 OKTAVIAN team of Osaka University for assisting in obtaining the neutron detector response; H.
392 Tomita and A. Uritani of Nagoya University, S. Conroy, L. Giacomelli, and V. Kiptily of Culham
393 Centre for Fusion Energy, A. L. Roquemore and the late D. S. Darrow of Princeton Plasma Physics
394 Laboratory, G. Q. Zhong of the Chinese Institute of Plasma Physics, and T. Itoh of Kitano
395 Manufacturing Corp. in discussing the design of a multichannel collimator and detectors; T. Honda
396 and M. Goto of G-tech Corp. in discussing the PSD ability of the scintillator; A. Okada of

397 Hamamatsu Photonics K.K. in providing background knowledge of the photomultiplier; T. Takada of
398 National Institute of Technology, Ariake College and S. Yoshimura of National Institute for Fusion
399 Science in assisting with PMT test using LED; E. Takada of National Institute of Technology,
400 Toyama college, M. Riva, D. Marocco, B. Esposito, B. Francesco of the Italian National Agency for
401 New Technologies, Energy and Sustainable Economic Development in discussing the FPGA logic;
402 and Y. Endo, F. Watanabe, and Y. Arai of Techno AP for joint development of the FPGA circuit.
403

404 References

- 405 ¹O. N. Jarvis Plasma Phys. Control. Fusion **36** 209 (1994).
- 406 ²J. D. Strachan, A. Bhattacharjee, D. J. Jassby, and H. H. Towner, Phys. Lett. **66A** 295 (1978).
- 407 ³A. L. Roquemore, R. C. Chouinard, M. Diesso, R. Palladino, J. D. Strachan, and G. D. Tait, Rev.
- 408 Sci. Instrum. **61** 3163 (1990).
- 409 ⁴A. L. Roquemore, M. Bitter, L. C. Johnson, and S. von Goeler, Rev. Sci. Instrum. **68** 544 (1997).
- 410 ⁵L. C. Johnson, Rev. Sci. Instrum. **63** 10 (1992).
- 411 ⁶J.M. Adams, O.N. Jarvis, G.J. Sadler, D.B. Syme, N. Watkins, Nucl. Instrum. Meth. A **329** 277
- 412 (1993).
- 413 ⁷M. Riva, B. Esposito, D. Marocco, F. Belli, B. Syme, L. Giacomelli, Fus. Eng. and Design **86** 1191
- 414 (2011).
- 415 ⁸T. Craciunescu, G. Bonheure, V. Kiptily, A. Murari, S. Soare, I. Tiseanu, V. Zoita, and JET EFDA
- 416 Contributors, Nucl. Instrum. and Meth. A **595** 623 (2008).
- 417 ⁹M. Ishikawa, T. Nishitani, A. Morioka, M. Takechi, K. Shinohara, M. Shimada, Y. Miura, M.
- 418 Nagami, and Yu. A. Kaschuc, Rev. Sci. Instrum. **73** 4237 (2002).
- 419 ¹⁰M. Ishikawa, T. Itoga, T. Okuji, M. Nakhostin, K. Shinohara, T. Hayashi, A. Sukegawa, and M.
- 420 Baba, Rev. Sci. Instrum. **77** 10E706 (2006).

421 ¹¹M. Ishikawa, M. Takechi, K. Shinohara, Y. Kusama, C.Z. Cheng, G. Matsunaga, Y. Todo, N.N.
422 Gorelenkov, G.J. Kramer, R. Nazikian, A. Fukuyama, V.A. Krasilnikov, Yu. Kashuck, T. Nishitani,
423 A. Morioka, M. Sasao, M. Isobe and the JT-60 team, Nucl. Fusion **45** 1474 (2005).

424 ¹²P. Batistoni, B. Esposito, M. Martone, and S. Mantovani, Rev. Sci. Instrum. **66** 4949 (1995).

425 ¹³M. Cecconello, M. Turnyanskiy, S. Conroy, G. Ericsson, E. Ronchi, S. Sangaroon, R. Akers, I.
426 Fitzgerald, A. Cullen, and M. Weiszflog, Rev. Sci. Instrum. **81** 10D315 (2010).

427 ¹⁴Joung-Gu Kwak, H. S. Kim, M. S. Cheon, S. T. Oh, Y. S. Lee, T. Terzolo, and KSTAR team,
428 Fusion Eng. Des. **109-111** 608 (2016).

429 ¹⁵ Y. Izumi, H. Tomita, Y. Nakayama, S. Hayashi, K. Morishima, M. Isobe, M. S. Cheon, K. Ogawa,
430 T. Nishitani, T. Naka, T. Nakano, M. Nakamura, and T. Iguchi, Rev. Sci. Instrum. **87** 11D840 (2016).

431 ¹⁶G. Q. Zhong, L. Q. Hu, N. Pu, R. J. Zhou, M. Xiao, H. R. Cao, Y. B. Zhu, K. Li, T. S. Fan, X. Y.
432 Peng, T. F. Du, L. J. Ge, J. Huang, G. S. Xu, B. N. Wan, EAST Team, Rev. Sci. Instrum. **87** 11D820
433 (2016).

434 ¹⁷Y. P. Zhang, J. W. Yang, Yi Liu, T. S. Fan, X. B. Luo, G. L. Yuan, P. F. Zhang, X. F. Xie, X. Y.
435 Song, W. Chen, X. Q. Ji, X. Li, T. F. Du, L. J. Ge, B. Z. Fu, M. Isobe, X. M. Song, Z. B. Shi, Q. W.
436 Yang, X. R. Duan, Rev. Sci. Instrum. **87** 063503 (2016).

437 ¹⁸W. J. Capecchi, J. K. Anderson, P. J. Bonofiglio, J. Kim, S. Sears, Rev. Sci. Instrum. **87** 11D826
438 (2016).

439 ¹⁹M. Cecconello, S. Sangaroon, M. Turnyanskiy, S. Conroy, I. Wodniak, R.J. Akers, G. Ericsson and
440 the MAST Team, Nucl. Fusion **52** 094015 (2012).

441 ²⁰L. Giacomelli, A. Hjalmarsson, H. Sjostrand, W. Glasser, J. Kallne, S. Conroy, G. Ericsson, M.
442 Gatu Johnson, G. Gorini, H. Henriksson, S. Popovichev, E. Ronchi, J. Sousa, E. Sunden Andersson,
443 M. Tardocchi, J. Thun, M. Weiszflog and Contributors to the JET-EFDA Workprogram, Nucl. Fusion
444 **45** 1191 (2005).

445 ²¹D. Marocco, B. Esposito and F. Moro, JINST **7** C03033 (2012).

446 ²²M. Sasao, M. Isobe, M. Osakabe, A. Taniike, T. Iguchi, H. Takada, T. Iida, and M. Wada, Fusion
447 Eng. Design **34** 595 (1997).

448 ²³X-5 Monte Carlo Team, “MCNP - A General N-Particle Transport Code, Version 5”, Volume I:
449 Overview and Theory LA-UR-03-1987 (2003, updated 2005).

450 ²⁴M. Isobe, H. Yamanishi, M. Osakabe, H. Miyake, H. Tomita, K. Watanabe, H. Iwai, Y. Nomura, N.
451 Nishio, K. Ishii, J. H. Kaneko, J. Kawarabayashi, E. Takada, A. Uritani, M. Sasao, T. Iguchi, Y.
452 Takeiri, and H. Yamada, Rev. Sci. Instrum. **81** 10D310 (2010).

453 ²⁵K. Ogawa, M. Isobe, E. Takada, Y. Uchida, K. Ochiai, H. Tomita, A. Uritani, T. Kobuchi, and Y.
454 Takeiri, Rev. Sci. Instrum **85** 11E110 (2014).

455 ²⁶H. Kawase et al., accepted for publication in IEEE transaction of plasma physics

456 ²⁷https://www.hamamatsu.com/resources/pdf/etd/R11265U_H11934_TPMH1336E.pdf

457 ²⁸<http://www.hongsencable.com/pdf/01714670.pdf>

458 ²⁹<https://www.tek.com/datasheet/digital-phosphor-oscilloscopes>

459 ³⁰http://www.techno-ap.com/img/APV8102_14MWPSAGb.pdf

460 ³¹<http://www.techno-ap.com/img/APV3304.pdf>

461 ³²<https://www.matsusada.com/product/psel/dcps/handy/000002/>

462 ³³<http://netgear.com/business/products/switches/smart/XS712T.aspx>

463 ³⁴M. Y. Tanaka, M. Aramaki, K. Ogiwara, S. Etoh, S. Yoshimura, and J. Varanjes., AIP Conference

464 Proceedings **1061** 57 (2008).

465 ³⁵https://www.nfcorp.co.jp/english/sup/dl/manual/mi/e_wf1946b.pdf

466 ³⁶K. Ishii, K. Shinohara, M. Ishikawa, M. Baba, M. Isobe, A. Okamoto, S. Kitajima, and M. Sasao,

467 Rev. Sci. Instrum. **81** 10D334 (2010).

468 ³⁷C. Konno, Compendium of Neutron Beam Facilities for High Precision Nuclear Data

469 Measurements IAEA-TECDOC-1743 (Vienna: IAEA) pp 110–18 ([https://www-](https://www-nds.iaea.org/publications/tecdocs/iaea-tecdoc-1743/)

470 [nds.iaea.org/publications/tecdocs/iaea-tecdoc-1743/](https://www-nds.iaea.org/publications/tecdocs/iaea-tecdoc-1743/)) (2014).

471 ³⁸[https://eng.surugaseiki.com/Products/spec/Motorized+Stage/Motorized+Linear+Stage/X-](https://eng.surugaseiki.com/Products/spec/Motorized+Stage/Motorized+Linear+Stage/X-Axis+Motorized+Stage/KXL06300/KXL06300-N2-F3C/pkey:X-Axis%20Motorized%20Stage%20%E2%96%A160)

472 [Axis+Motorized+Stage/KXL06300/KXL06300-N2-F3C/pkey:X-](https://eng.surugaseiki.com/Products/spec/Motorized+Stage/Motorized+Linear+Stage/X-Axis+Motorized+Stage/KXL06300/KXL06300-N2-F3C/pkey:X-Axis%20Motorized%20Stage%20%E2%96%A160)

473 [Axis%20Motorized%20Stage%20%E2%96%A160](https://eng.surugaseiki.com/Products/spec/Motorized+Stage/Motorized+Linear+Stage/X-Axis+Motorized+Stage/KXL06300/KXL06300-N2-F3C/pkey:X-Axis%20Motorized%20Stage%20%E2%96%A160)

474 ³⁹<http://www.caen.it/csite/CaenProd.jsp?parent=14&idmod=632>

475 ⁴⁰<http://www.ni.com/ja-jp/support/model.ni-5772.html>

476 ⁴¹<http://www.ni.com/ja-jp/support/model.pxie-7962.html>

477 ⁴²M. Baba, M. Takada, T. Iwasaki, S. Matsuyama, T. Nakamura, H. Ohguchi, T. Nakano, T. Sanami,
478 and N. Hirakawa, Nucl. Instrum. Methods Phys. Res. A **376** 115 (1996).

479 ⁴³I. Murata Compendium of Neutron Beam Facilities for High Precision Nuclear Data Measurements
480 IAEA-TECDOC-1743 (Vienna: IAEA) pp 110–18 ([https://www-](https://www-nds.iaea.org/publications/tecdocs/iaea-tecdoc-1743/)
481 [nds.iaea.org/publications/tecdocs/iaea-tecdoc-1743/](https://www-nds.iaea.org/publications/tecdocs/iaea-tecdoc-1743/)) (2014).

482 ⁴⁴I. Yamada, K. Narihara, H. Funaba, T. Minami, H. Hayashi, T. Kohmoto and LHD Experiment
483 Group, Fusion Sci. Technol. **58** 353 (2010).

484 ⁴⁵T. Akiyama et al., Fusion Sci. Technol. **58** 345 (2010).

485 ⁴⁶M. Isobe et al., Rev. Sci. Instrum. **85** 11E114 (2014).

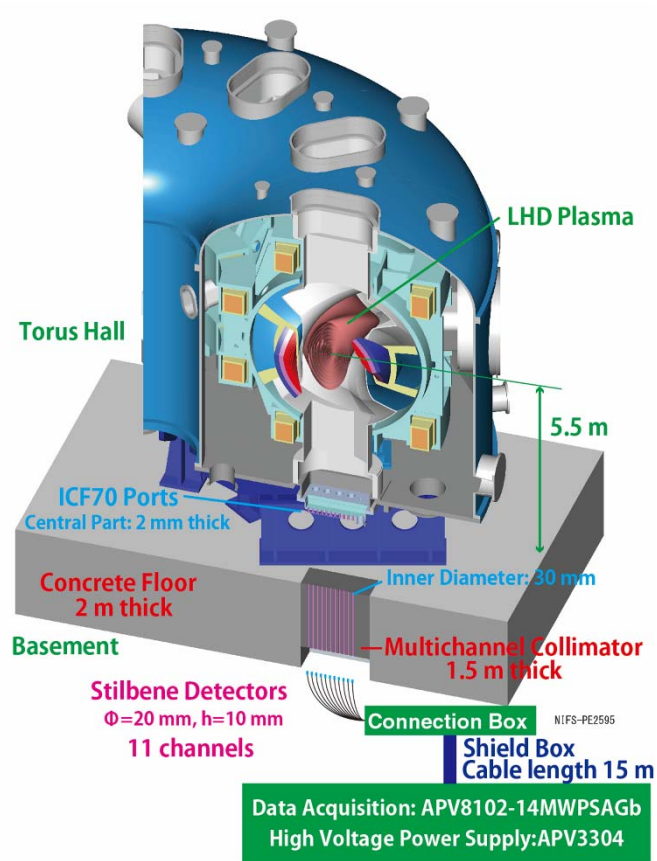
486

487 Table 1 Weight ratio of heavy concrete material

Chemical composition	Weight ratio (%)
H ₂ O	3.3
SiO ₂	1.2
Al ₂ O ₃	0.28
Fe ₂ O ₃	91
CaO	3.8
MgO	0.084
SO ₃	0.17
Na ₂ O	0.015
K ₂ O	0.022
Cl	0.00029

488

489

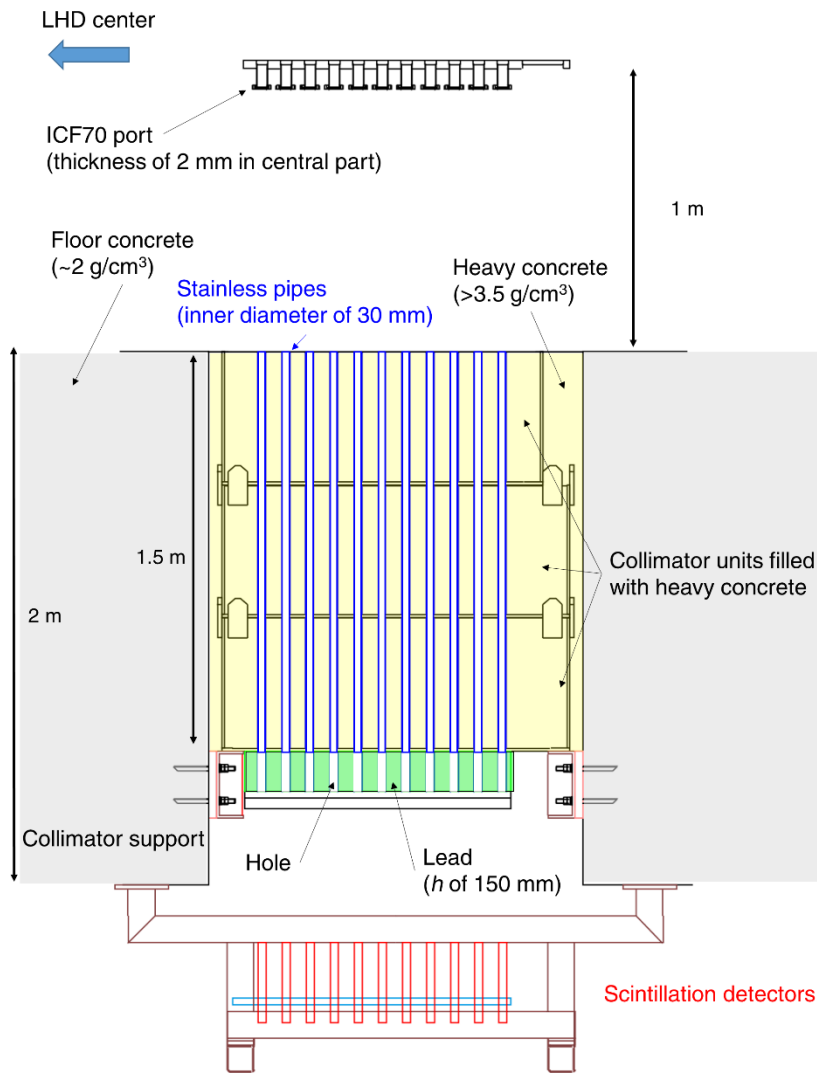


490

491 Fig.1 Schematic drawing of LHD vertical neutron camera

492

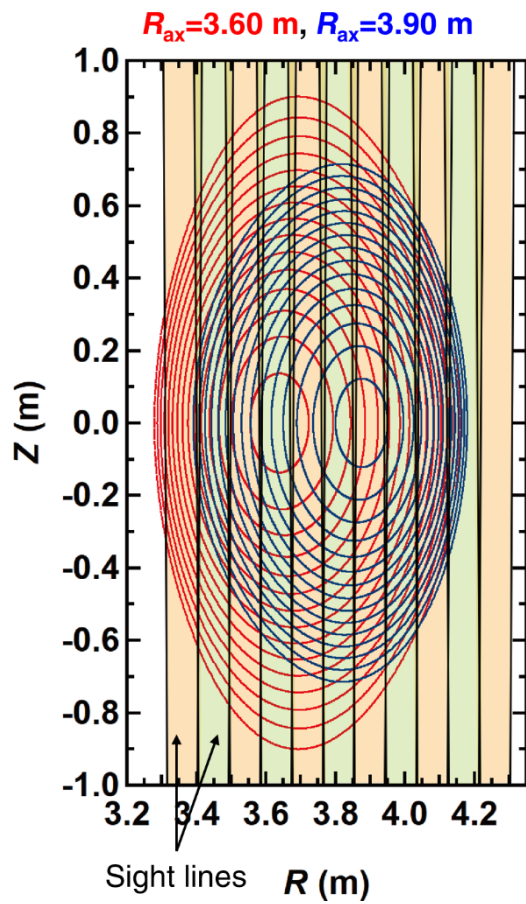
493



494

495 Fig.2 Schematic of the ports, the multichannel collimator, and the detector support of LHD VNC.

496

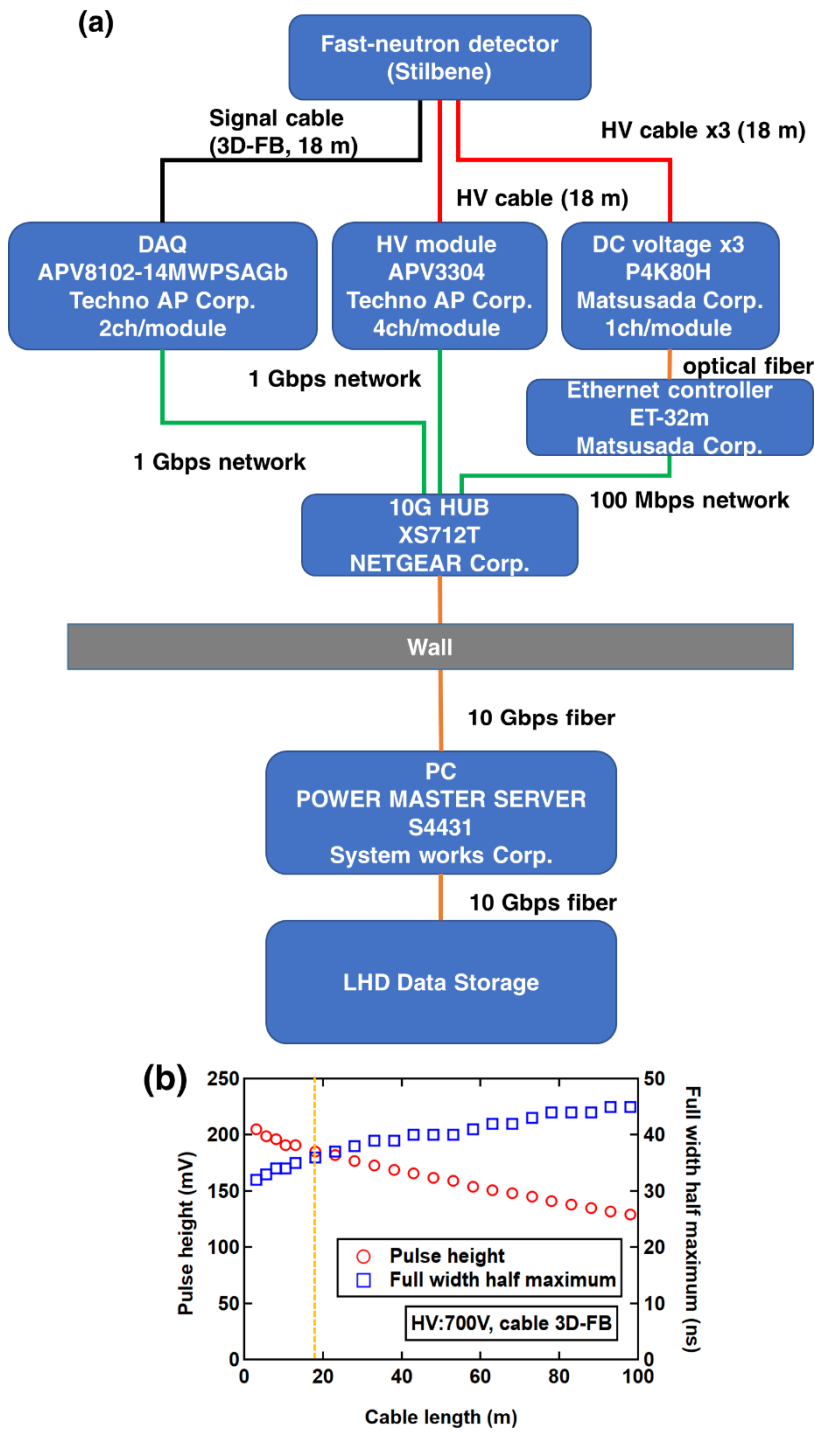


497

498 Fig.3 Sight lines of VNC and poloidal cross section of plasma with R_{ax} of 3.60 m and 3.90 m with zero

499 beta. The diameter of each sight line is 88 mm at Z of -0.9 m and 110 mm at Z of 0.9 m.

500

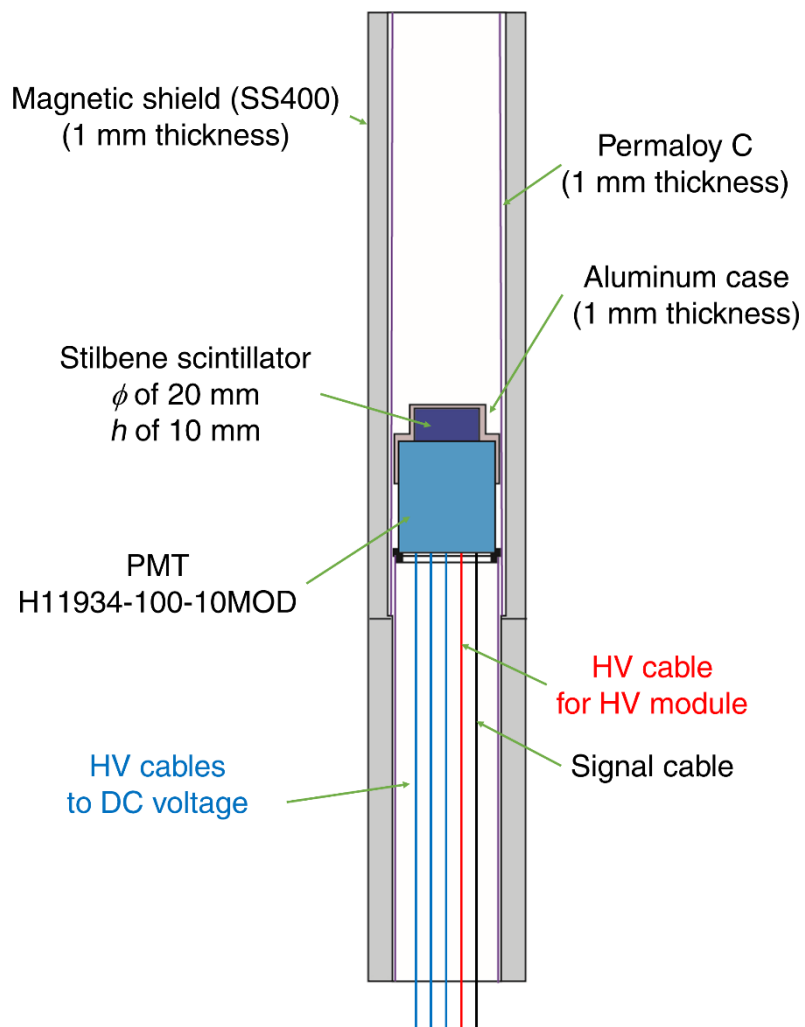


501

502 Fig.4 (a) Electronic schematic of VNC. All the electrical components are externally controllable. (b)

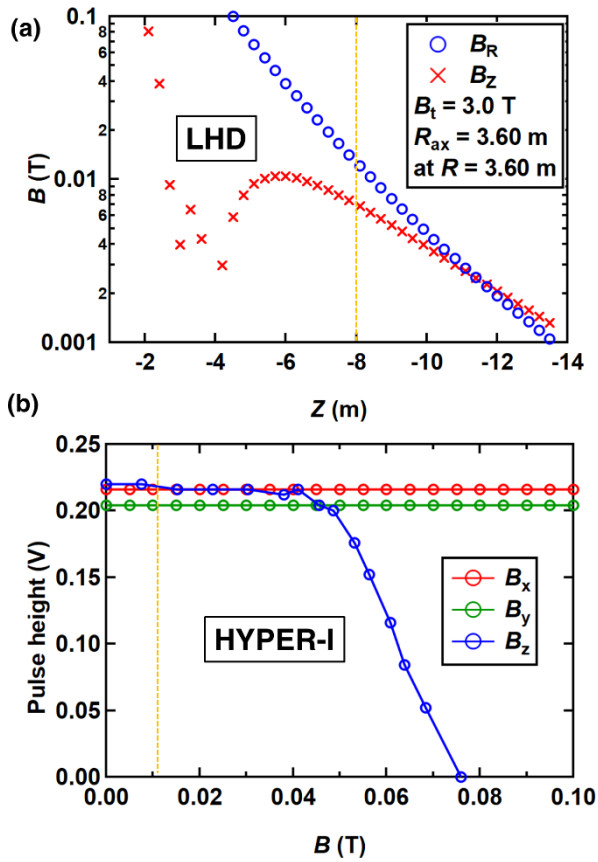
503 Pulse height and pulse width as a function of cable length.

504



505

506 Fig.5 Schematic drawing of the fast-neutron detector.



507

508 Fig.6 (a) Typical profile of magnetic field strength at the vertically elongated cross section in LHD

509 where B_t , R_{ax} , Z , and R represent the toroidal magnetic field strength, the plasma major radius, the

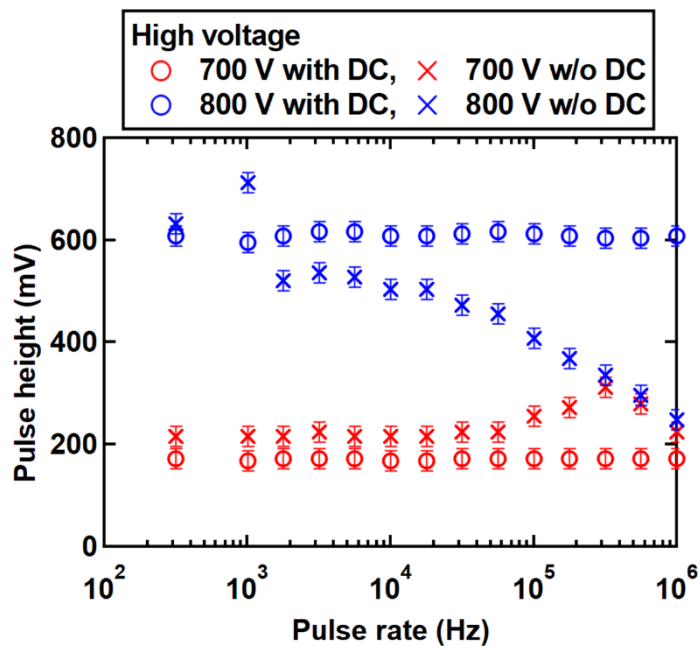
510 height from the plasma plane, the major radius from the machine center, respectively. The dashed

511 line shows the location of fast-neutron detectors. (b) Test of the magnetic shield in HYPER-I. The

512 dashed line shows the magnetic field strength at the fast-neutron detector position. The magnetic

513 shield has sufficient performance as designed.

514



515

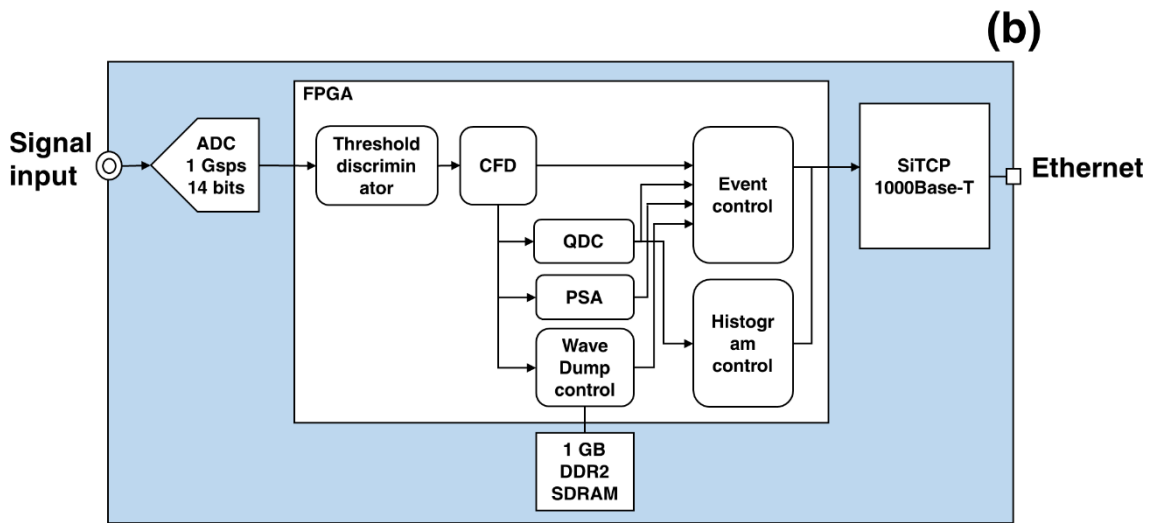
516 Fig. 7 Result of gain stability. The gain of PMT is not changed even at 10⁶ cps with external DC

517 power supplies.



Manufactury: Techno AP Corp.
 Model: APV8102-14MWPSAGb
 Input impedance: 50 Ohm
 Sampling Freq. : 1 GHz
 Number of channels : 2 ch
 No. of bits : 14
 V_{pp} : 2 V or 6 V
 Bandwidth : 500 MHz
 Transfer rate : ~120 MB/s (1 Gbps)
 DRAM : 1 GB x 2
 FPGA

(a)



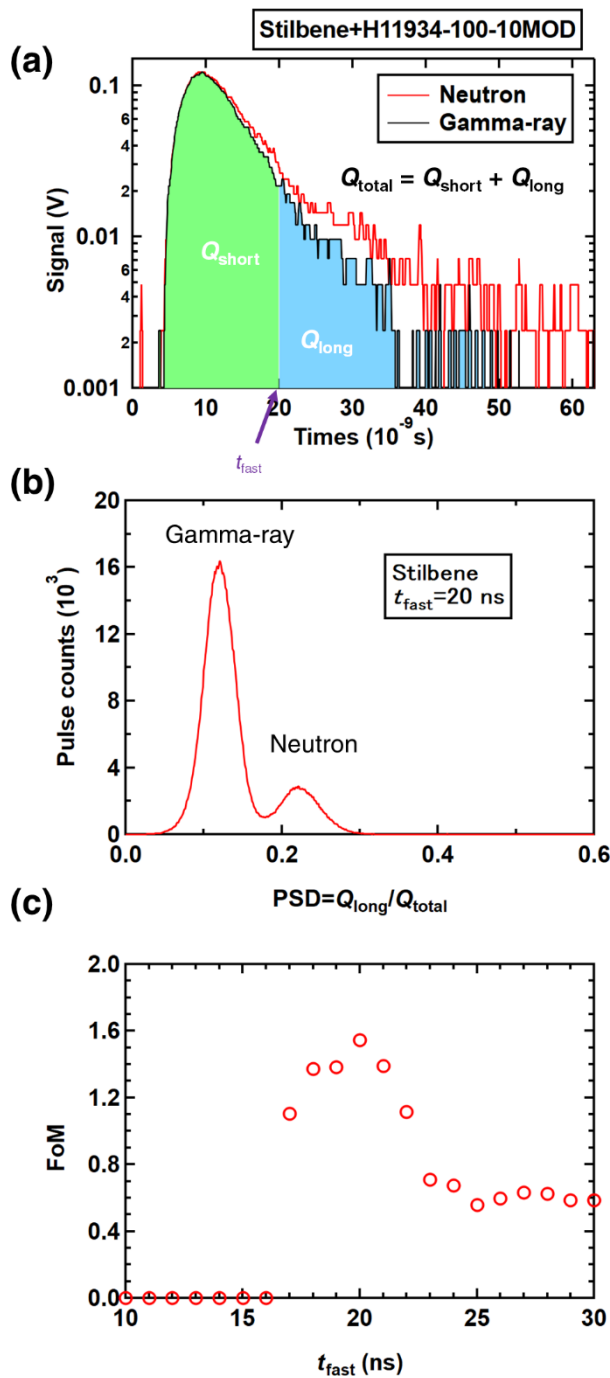
(b)

519

520 Fig.8 (a) Specification of DAQ for LHD VNC. (b) Electronic schematic of the DAQ. The data is

521 stored in the internal memory and transferred after the discharge.

522



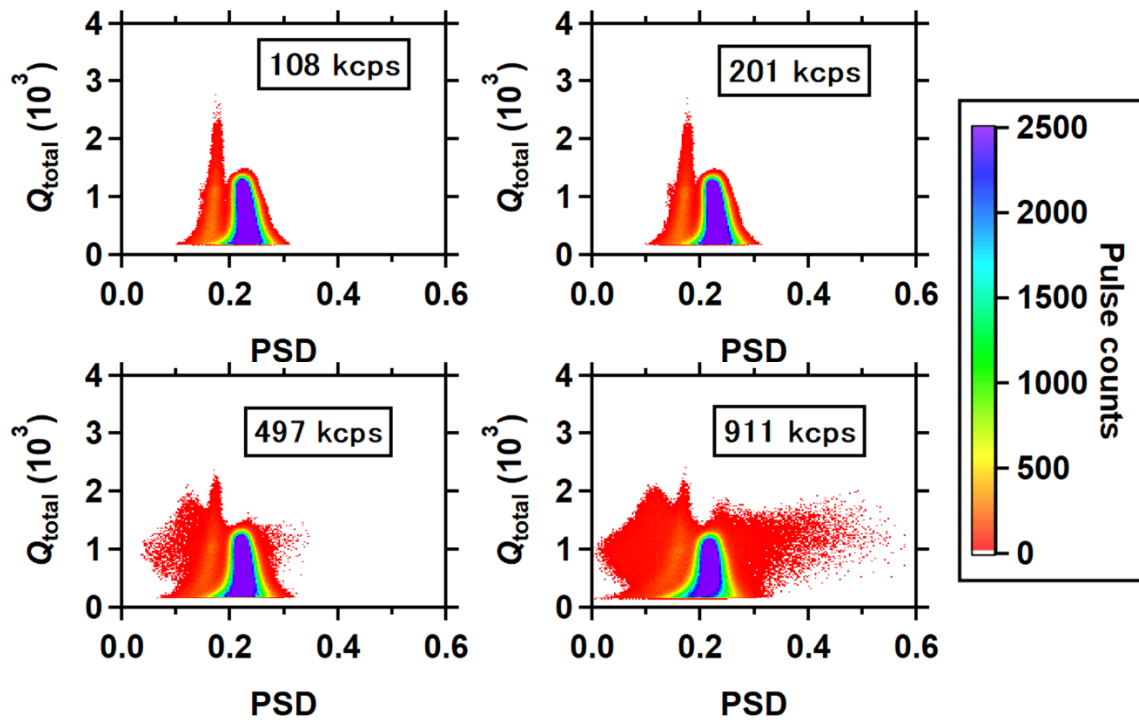
523

524 Fig. 9 (a) Typical signal of the fast-neutron detector induced by fast-neutron and gamma-ray. The

525 decay time of the signal is longer in the fast-neutron case compared with gamma-rays. (b) Typical

526 one-dimensional histogram of pulse shape discrimination for stilbene detector. (c) Pulse shape

527 discrimination ability as a function of t_{fast} . The highest FoM is obtained at a t_{fast} of around 20 ns.

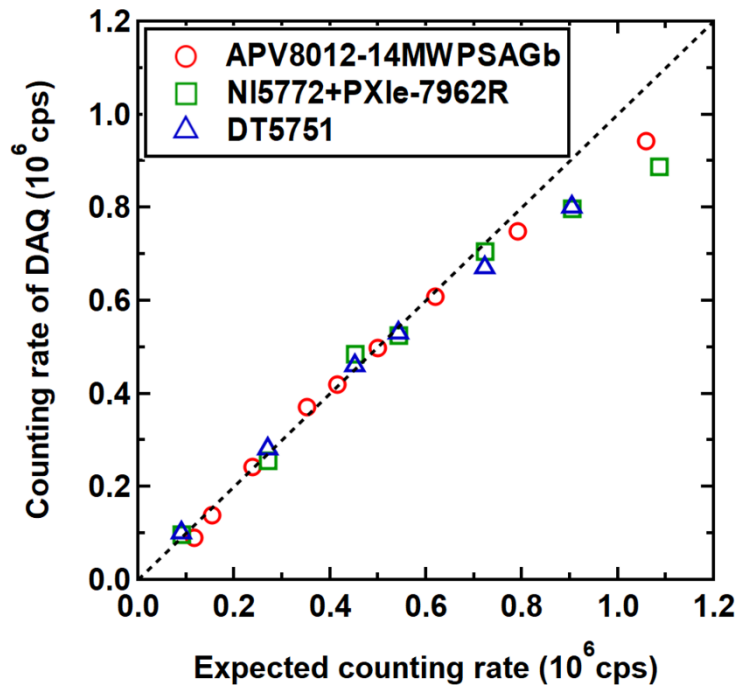


528

529 Fig. 10 Two dimensional pulse shape discrimination plots in different counting rates obtained in the

530 FNS. Here, $\text{PSD} = Q_{\text{long}} / Q_{\text{total}}$. The map appears to be stable regardless of the counting rate.

531

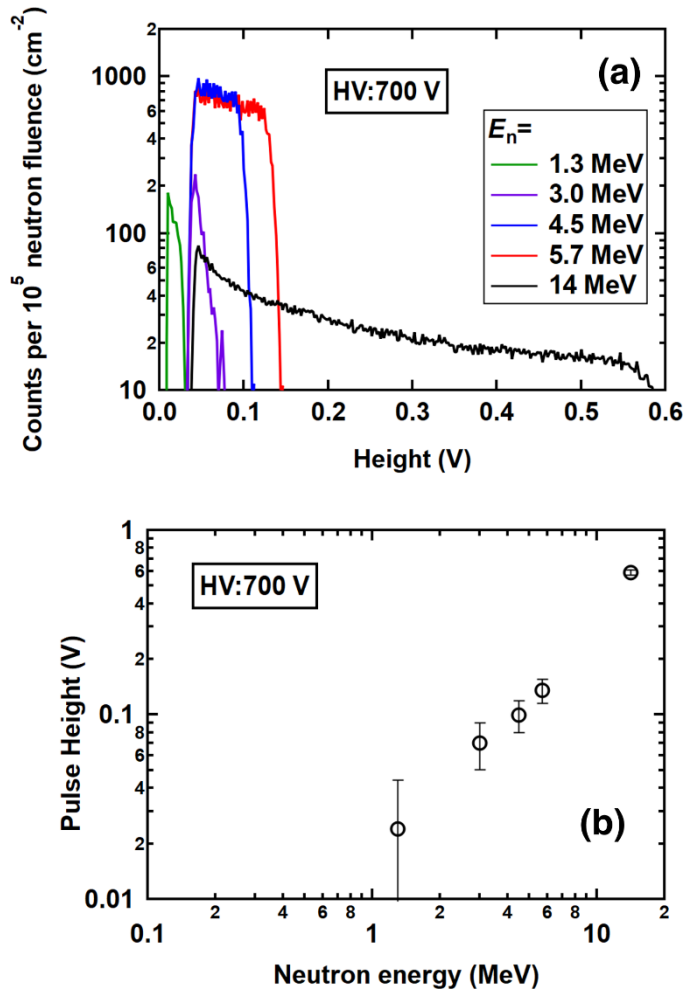


532

533 Fig. 11 Pulse counting rate obtained with DAQ as a function of expected counting rate evaluated by

534 the neutron flux at the detector position in the FNS. The counting loss ratio of APV8102-

535 14MWPSAGb is minimum among three DAQs.



536

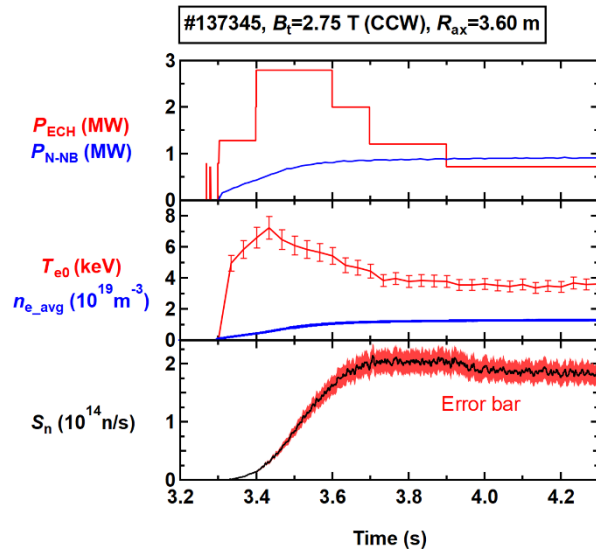
537 Fig. 12 (a) Pulse height spectra obtained at the neutron energy of 1.3 MeV, 3.0 MeV, 4.5 MeV, 5.7

538 MeV, and 14 MeV. (b) The maximum pulse height as a function of neutron energy. The pulse height

539 monotonically increases with neutron energy as expected.

540

541

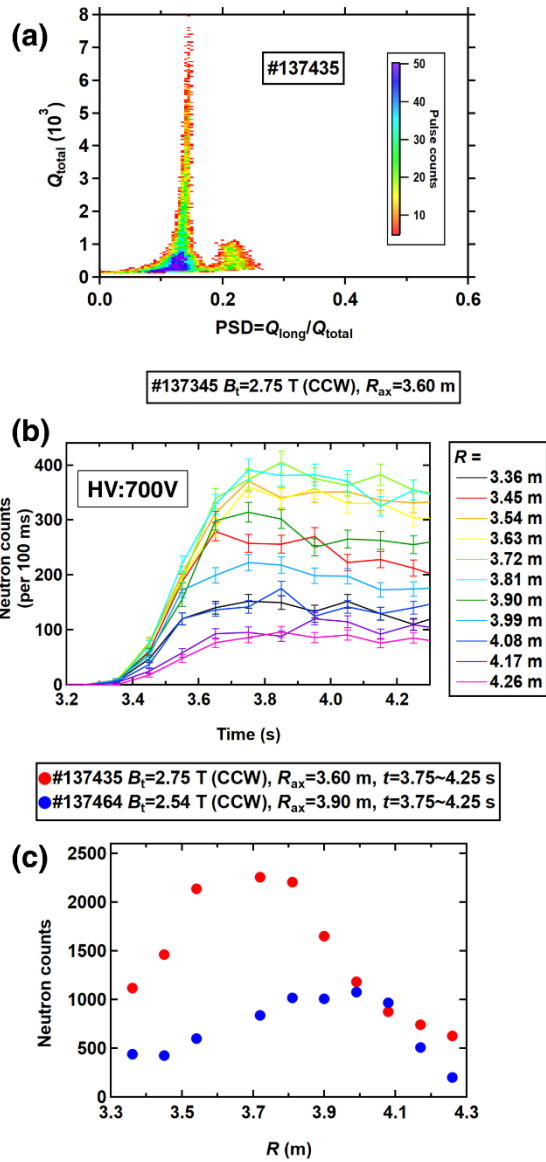


542

543 Fig. 13 Typical time trace of electron cyclotron heated (ECH) and negative-ion-based neutral beam

544 (N-NB) injected plasma discharge.

545



546

547 Fig. 14 (a) Typical two-dimensional pulse shape discrimination plot obtained in the LHD

548 experiment. (b) Typical time traces of the line-integrated neutron emission profile. (c) Typical line-

549 integrated neutron emission profile obtained at R_{ax} of 3.60 m and 3.90 m. Number of neutron count

550 decreases with the outward shift of R_{ax} which is consistent with the total neutron emission rate

551 measurement. The peak position of the profile shifted outward with R_{ax} as expected.

552

(a)



(b)



554

555 Fig. 15 (a) Three multichannel collimator units. (b) The multichannel collimator made in the LHD

556 torus hall.